

---

## **Integrated design of an AGV for improved GPS-based path-following performance**

---

Mathieu Joerger\*, John Christ,  
Richard Duncan and Boris Pervan

Mechanical, Materials and Aerospace Engineering Department,  
Illinois Institute of Technology, 10W 32nd Street, Chicago,  
IL 60616, USA

E-mail: joermat@iit.edu E-mail: JohnChrist@Precoat.com

E-mail: duncric@iit.edu E-mail: pervan@iit.edu

\*Corresponding author

**Abstract:** This paper describes the design, simulation and testing of an automated ground vehicle intended to perform trajectory-tracking operations using GPS as primary sensor. Its development results from the integrated design of the vehicle with its navigation, guidance and control system. This integrated design process is oriented toward directly maximising the trajectory-tracking performance, rather than individually optimising secondary mechanical performance characteristics, as in more traditional methods. Detailed covariance analyses and closed-loop simulations are carried out to evaluate the ultimate dynamic performance and to quantify the impact of each vehicle parameter. In particular, the performance sensitivity is analysed with respect to parameters for which no obvious selection criteria exists, such as the vehicle's sense of motion or the positioning sensor location, which prove to be decisive characteristics. Experimental testing on a prototype rover confirms the simulations' results and validates the selection of the vehicle design parameters.

**Keywords:** automated; control; GPS; integrated design; navigation.

**Reference** to this paper should be made as follows: Joerger, M., Christ, J., Duncan, R. and Pervan, B. (2006) 'Integrated design of an AGV for improved GPS-based path-following performance', *Int. J. Vehicle Design*, Vol. 42, Nos. 3/4, pp.263–286.

**Biographical notes:** Mathieu Joerger is a PhD student in Mechanical and Aerospace Engineering at the Illinois Institute of Technology (IIT) in Chicago. In 2002, he obtained a Masters in Mechatronics at the Ecole Nationale Supérieure des Arts et Industries de Strasbourg (France) and a MS in Mechanical and Aerospace Engineering at IIT. He is currently working as a research assistant on the integration of GPS with auxiliary navigation systems for applications on autonomous ground vehicles.

John Christ currently works as a Project Engineer. In 1989, he obtained a Bachelors Degree (BS) in Engineering Science from Iowa State University in Ames, Iowa and in 2003, a Master of Science Degree (MS) in Mechanical and Aerospace Engineering from IIT. His Thesis work at IIT included developing an autonomous ground vehicle and testing the GPS based navigation system.

Richard Duncan is a MS student in Finance at IIT's Stuart Graduate School of Business. He graduated with a BS in Aerospace Engineering from IIT in May of 2005. He held research positions with IIT's Navigation and Guidance Lab as well as the Fluid Dynamics Research Center's National Diagnostic Facility and NASA's Kennedy Space Center during his undergraduate career.

Dr. Boris Pervan is an Associate Professor of Mechanical and Aerospace Engineering at the Illinois Institute of Technology (IIT) in Chicago. He received his BS from the University of Notre Dame, MS from the California Institute of Technology, and PhD from Stanford University. He was the recipient of the IIT/Sigma Xi Excellence in University Research Award (2005), University Excellence in Teaching Award (2005), Ralph Barnett Mechanical and Aerospace Engineering Dept. Outstanding Teaching Award (2002), IEEE M. Barry Carlton Award (1999), RTCA William E. Jackson Award (1996), and is currently an Associate Editor of the journal *Navigation*.

---

## 1 Introduction

This article introduces and demonstrates a procedure to optimise the path-following performance of an autonomous vehicle system using differential global positioning system (DGPS) navigation. In traditional applications of this type, the navigation, guidance and control system is designed and built for an existing vehicle. In contrast, in this work we carry out an *integrated* design of the vehicle with its controller. The integrated design process is oriented toward directly maximising the path-following performance, rather than individually optimising secondary vehicle mechanical performance characteristics, such as the operating velocity. Using this method, system performance is maximised, and unnecessary and costly additional equipment or over-sized components can be avoided.

### 1.1 Focus

Automated ground vehicles (AGVs) can support a variety of highly-detailed missions that are unsafe or too difficult for human operation. In 1997, O'Connor (1997), whose work was later refined by Bell (1999), set the path for the development and expansion of DGPS-based automated vehicle control techniques in practical applications. He successfully realised the automated control of a tractor using carrier-phase differential GPS (CDGPS) for unmanned agricultural field ploughing. Since then, in less than a decade, precision-controlled AGVs have been successfully implemented in outdoor applications such as ramming of ski runs (Opshaug and Enge, 2000), topographic field mapping, handling of hazardous materials, lawn mowing and more (Hannu, 2001).

Advances in sensor technologies have contributed greatly to these successes. The global positioning system (GPS) is a particularly well-suited sensor for outdoor navigation purposes, as illustrated by Abbott's comparative study of existing navigation sensors (Abbott and Powell, 1999). More precisely, CDGPS provides centimetre-level accuracy, which is critical for many precision applications of

automated land vehicles. Positioning using CDGPS is based on the use of a GPS carrier phase ranging measurements between the rover and the satellites, and corrections sent in real-time by a fixed reference station through a data link. If the carrier phase cycle ambiguities are correctly resolved, the accuracy of the positioning measurements is close to 1 cm root-mean-square, depending on satellite geometry and multipath conditions (Misra et al., 1999).

### *1.2 Motivation*

For trajectory-tracking operations, the measurement update rate is a decisive parameter since it determines the frequency of the vehicle course corrections. Especially, when using CDGPS as the only sensor, the limited sample period gives rise to a trade-off between vehicle velocity and path-following performance. Multisensor systems, such as the CDGPS aided inertial navigation system (INS) implemented by Farrell et al. (2003), demonstrate higher sample rates. But the actuators' dynamic response also impacts the efficiency of the course corrections, so that the sensors and actuators' bandwidths should be selected accordingly. Traditionally, the optimal choice of such system components and parameters for a specific mission requires prior experience, which is not always available.

In response, we carry out an integrated design process, which establishes the relationship between vehicle parameters, including sensor and actuator characteristics, and path-following performance. The process requires that detailed parametric models for both the vehicle and the controller be coherently derived. Performance predictions are then estimated before the vehicle is built, allowing for an optimal selection of the vehicle design parameters.

### *1.3 Outline of the paper*

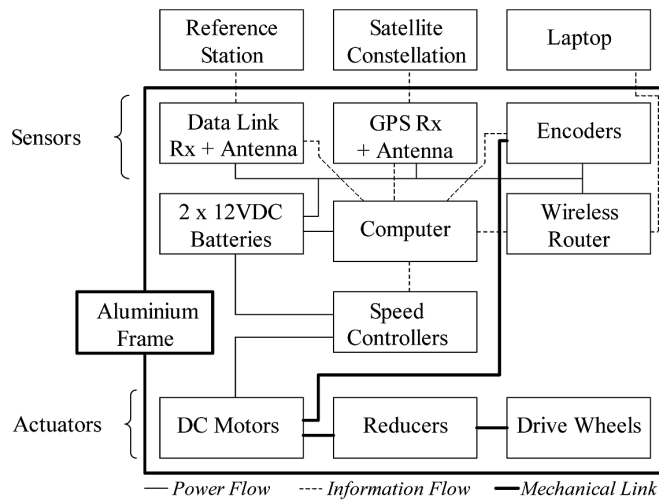
To illustrate this idea, we designed, built and tested a prototype AGV called 'Leonard'. In this paper, the Leonard platform serves as a benchmark example of the role of navigation and control system analysis in the identification and optimisation of critical vehicle design parameters. Vehicle requirements and basic characteristics, such as the sense of motion and operating velocity, are selected for the desired trajectory-tracking performance. In addition, detailed covariance analyses and closed-loop simulations are carried out to evaluate the ultimate dynamic performance and to quantify the impact of specific vehicle design parameters. In this regard, the performance sensitivity can even be analysed with respect to parameters for which no obvious selection criteria exists. In particular, the positions of the GPS antenna (positioning sensor location) and of the control point (the point on the AGV designated to follow the predefined trajectory) prove to be decisive parameters. Experimental testing supports the predicted results, confirms the vehicle parameter selection, and validates the design process.

The Leonard platform is the first of a series of mobile units intended to operate as a coordinated network for the study of distributed vehicle control. Since it will be duplicated, its design is of prime interest. The procedure followed for Leonard's development is presented here.

## 2 Baseline vehicle design

To provide a simple, robust framework for the vehicle system analysis and design, we focus on a differential drive AGV concept. Steering is performed by a difference in angular velocity on two opposed driving wheels. Figure 1 gives an overview of the major vehicle components. In this section, the actuators and the aluminium frame's dimensions are pre-selected, because they are subject to mechanical constraints, which will be explained shortly. However, the positions of the sensor and control points in the final assembly, as well as the operating velocity, the sense of motion and the controller's update rate, are selected by analysis in the rest of the paper.

**Figure 1** Vehicle components



### 2.1 Vehicle components

The actuators are composed of two DC-motors with gear-and-belt type reducers linked to the driving wheels. They were selected coherently with the other components, in particular with the batteries, in order for the system to operate correctly. The total weight of the vehicle determines the size of the motors, which in turn fixes the battery requirements. An iterative process is used to confirm that the selected actuators together with their mounting elements (bearing, shafts, sprockets, etc.), selected from the available market supply, can move the weight of the total assembly (Christ, 2003).

The DGPS sensor is composed of a GPS receiver (NovAtel ProPakII), receiving signals from GPS satellites in view, and a spread spectrum data link in communication with the reference station. An important limitation on the DGPS system is its update rate. A practical lower limit for the sensor sample time based on the typical 10 Hz bandwidth of the GPS receiver tracking loops is 0.2 s. For a given operating velocity, this characteristic constitutes the main limiting factor for the update rate of the cross-track-error correction. The GPS patch-antenna is fixed at the centre of an aluminium plate in order to minimise the effects of multipath reflections.

Optical encoders are mounted on the motor's driving shaft but used only occasionally as an auxiliary sensor during testing.

Sensor data is processed by an embedded computer equipped with a data acquisition card, which sends commands to the motors via speed-controller interfaces. The purpose of the speed controllers is to provide to the motors the necessary amperage at the computer's request. Additionally, a wireless system provides remote-control capability, which is useful for testing. The power is delivered by two 12 V-DC batteries, which allow for up to 4 h of autonomous operation. All the components, with the exceptions of the antennae and the wheels, are enclosed in a waterproof and dust-proof rugged aluminium frame. Two floating casters are added to ensure vehicle balance and stability. Details on the selection of the components are available in Christ (2003).

## *2.2 Mechanical constraints*

The potential selection range for these components is limited by mechanical constraints. For example, the vehicle's length and width are limited by the size of the storage area; the actuators' selection, is dependent on numerous factors such as the weight, and the batteries amperage; also, the wheels and frame must be able to withstand the humidity and dust of the outdoor environment.

These mechanical criteria, and the vehicle velocity requirement (left as a parameter here) form the basis of traditional vehicle design. In the context of automated navigation and guidance control, additional factors must be considered, as illustrated in the following sections.

## **3 Dynamic model**

A detailed dynamic model is necessary for the design of the controller, and the simulation of Leonard's behaviour. It provides the basis for the parametrisation and optimisation of design elements for trajectory tracking. In the second part of this section, the open-loop poles of the resulting linearised system are analysed to select vehicle parameters such as the rover's sense of motion, or the position of its centre of mass.

With the differential-drive type of design selected, the vehicle can basically be modelled as a rectangular parallel pipe with two driving wheels and two floating casters. We assume that the wheels roll without slip, that the mass is uniformly distributed within the vehicle's body, and under the assumption that the ground is flat, we consider a two-dimensional model to be sufficiently accurate. Equations of motion for this non-holonomic system have been derived using traditional Newton-Euler methods, and verified using Lagrange's and Kane's equations (Joerger, 2002).

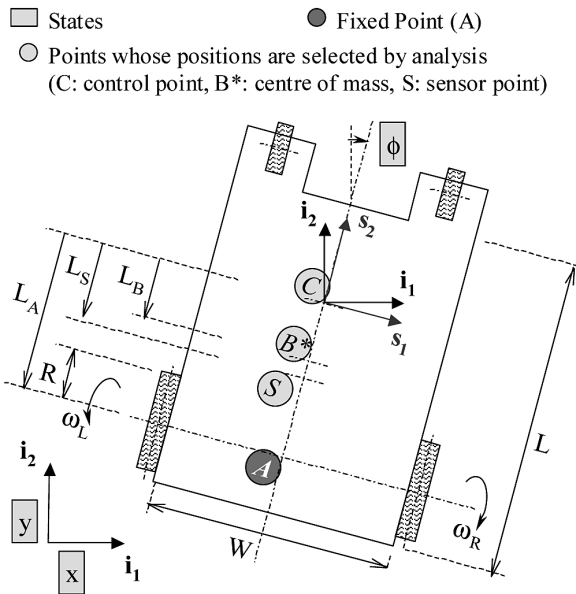
### *3.1 Equations of motion for the vehicle*

A complete list of parameters is given in Table 1 and illustrated in Figure 2.

**Table 1** Notations for the vehicle and the motors

Notations	Definition
$m$	mass of the vehicle
$W$	width of the vehicle
$L$	length of the vehicle
$R$	radius of the drive wheels
$L_A$	signed distance from point $C$ to point $A$
$L_B$	signed distance from point $C$ to point $B^*$
$L_S$	signed distance from point $C$ to point $S$
$J_{ZZ}$	moment of inertia of the vehicle's body at point $B^*$ about the vertical axis
$\mu_R$ and $\mu_L$	tension supplied to the right and left motors
$N$	reduction ratio
$k_T, k_E$	respectively torque and voltage constants
$R_a$	resistance in the rotor
$J$	moment of inertia for the rotor + reducer + wheels
$f_V$	damping coefficient associated with the rotor + reducer + wheels

**Figure 2** Top-view representation of the vehicle



The control point (point  $C$ ) is the point we want to remain on the predefined trajectory (e.g. if Leonard is used for land mine detection, it may designate the location of a magnetometer used to detect the mines). Its coordinates in the local inertial reference frame are  $x$  and  $y$ .  $\phi$  is the vehicle's heading angle.  $x$ ,  $y$ ,  $\phi$  and their

derivatives are the states of the forthcoming state space realisation. Note that point  $A$ , the intersection between the driving axle and the vehicle's principal axis, is the only intrinsically fixed point. Also,  $B^*$  indicates the vehicle's centre of mass. With the parameters described in the table, and with  $C_R$  and  $C_L$  being the torques on the right and left wheels respectively, we obtain:

$$m(\ddot{x} \sin \phi + \ddot{y} \cos \phi - \dot{\phi}^2 L_B) = \frac{C_R + C_L}{R} \quad (1)$$

$$\ddot{\phi}(J_{ZZ} - mL_B(L_A - L_B)) = m(L_A - L_B)(\ddot{x} \cos \phi - \ddot{y} \sin \phi) - \frac{WC_R - C_L}{2R} \quad (2)$$

and the constraint equation:

$$\dot{x} \cos \phi - \dot{y} \sin \phi + L_A \dot{\phi} = 0. \quad (3)$$

The constraint Equation (3) is representative of the fact that the vehicle's driving axle does not slip laterally. The sensor point (point  $S$ ) of coordinates  $x_S$  and  $y_S$ , designates the location of the GPS antenna; we have:

$$x_S = x + L_S \sin \phi \quad (4)$$

$$y_S = y + L_S \cos \phi. \quad (5)$$

Note that the signed parameters  $L_A$ ,  $L_B$  and  $L_S$  are referenced to the control point  $C$ . In consequence, terms such as  $(L_A - L_B)$  or  $(L_A - L_S)$  are not functions of the position of  $C$ , and represent the signed distance between  $A$  and  $B^*$  or  $A$  and  $S$ .

### 3.2 Model for the motors

Equations (1)–(5) are the equations of the model with torques as inputs. In practice, the actuators receive voltages as inputs. Therefore, a model of the motors, reducers and wheels is derived. We consider the mechanical and electrical equations commonly used to model DC-motors (Joerger, 2002). With  $\omega_{MR}$  and  $\omega_{ML}$ , the angular velocities on the right and left motors:

$$\omega_{MR} = \frac{N}{R} \left( \dot{x} \sin \phi - \dot{y} \cos \phi - \frac{W}{2} \dot{\phi} \right) \quad (6)$$

$$\omega_{ML} = \frac{N}{R} \left( \dot{x} \sin \phi - \dot{y} \cos \phi + \frac{W}{2} \dot{\phi} \right) \quad (7)$$

and under the assumption (verified for the class of motors selected) that the electromechanical time constant is small with respect to the other time constants, we obtain:

$$C_R = \frac{Nk_T}{R_a} u_R - \frac{N^2 J}{R} \left( \ddot{y} \cos \phi + \ddot{x} \sin \phi + \dot{\phi}(\dot{x} \cos \phi - \dot{y} \sin \phi) + \frac{W}{2} \ddot{\phi} \right) - \frac{N^2}{R} \left( \frac{k_T k_E}{R_a} + f_V \right) \left( \dot{y} \cos \phi + \dot{x} \sin \phi + \frac{W}{2} \dot{\phi} \right) \quad (8)$$

$$C_L = \frac{Nk_T}{R_a} u_L - \frac{N^2 J}{R} \left( \ddot{y} \cos \phi + \ddot{x} \sin \phi + \dot{\phi} (\dot{x} \cos \phi - \dot{y} \sin \phi) - \frac{W}{2} \ddot{\phi} \right) - \frac{N^2}{R} \left( \frac{k_T k_E}{R_a} + f_V \right) \left( \dot{y} \cos \phi + \dot{x} \sin \phi - \frac{W}{2} \dot{\phi} \right) \quad (9)$$

where the parameters are described in Table 1.

### 3.3 State space representation

Finally, the last four equations are combined to the model with torque-inputs. The resulting model is linearised at constant velocity ( $V_{y0}$ ) along a straight line, chosen to be the  $y$ -axis, and therefore assuming a small heading-angle  $\phi$ . In Section 5 of this work, we verify by using the non-linear model (Equations (1)–(5), (8) and (9)), that the linearisation hypothesis is valid for all the parameter values studied. We eventually obtain a complete linear dynamic model for the vehicle. In matrix form, we can deduce a multiple-input, multiple-output (MIMO) state space representation:

$$\begin{bmatrix} \ddot{y} \\ \ddot{\phi} \\ \dot{x} \\ \dot{y} + V_{y0} \\ \dot{\phi} \end{bmatrix} = \begin{bmatrix} \gamma & 0 & 0 & 0 & 0 \\ 0 & \alpha' & 0 & 0 & 0 \\ 0 & -L_A & 0 & 0 & V_{y0} \\ 1 & 0 & 0 & 0 & 0 \\ 0 & 1 & 0 & 0 & 0 \end{bmatrix} \begin{bmatrix} \dot{y} + V_{y0} \\ \dot{\phi} \\ x \\ y \\ \phi \end{bmatrix} + \begin{bmatrix} \zeta & \zeta \\ -\beta' & \beta' \\ 0 & 0 \\ 0 & 0 \\ 0 & 0 \end{bmatrix} \begin{bmatrix} u_R \\ u_L \end{bmatrix} \quad (10)$$

$$\begin{bmatrix} x_S \\ y_S \end{bmatrix} = \begin{bmatrix} 0 & 0 & 1 & 0 & L_S \\ 0 & 0 & 0 & 1 & 0 \end{bmatrix} \begin{bmatrix} \dot{y} + V_{y0} \\ \dot{\phi} \\ x \\ y \\ \phi \end{bmatrix} \quad (11)$$

with:

$$\gamma = -2N^2 \frac{f_V + k_T k_E / R_a}{mR^2 + 2N^2 J} \quad (12)$$

$$\zeta = \frac{RNk_T}{(mR^2 + 2N^2 J)R_a}$$

$$\alpha' = \frac{\alpha R^2 - \beta W N^2 (f_V + k_T k_E / R_a)}{R^2 + \beta N^2 J W} \quad (13)$$

$$\alpha = \frac{m(L_A - L_B)V_{y0}}{J_{ZZ} + m(L_A - L_B)^2}$$

$$\beta' = \frac{\beta RNk_T}{(R^2 + \beta N^2 J W)R_a}$$

$$\beta = \frac{W}{2(J_{ZZ} + m(L_A - L_B)^2)} \quad (14)$$

$$J_{ZZ} = \frac{1}{12} m(L^2 + W^2).$$

For notation purposes, one can recognise by identification the elements of a typical state space representation, expressed in the form of respectively the input and output equations:

$$\dot{\mathbf{x}} = F\mathbf{x} + G\mathbf{u}$$

$$\mathbf{y} = H\mathbf{x}$$

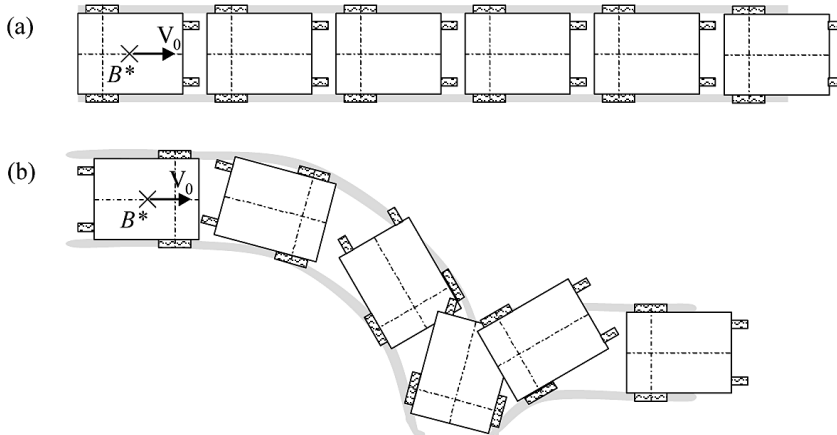
where  $\mathbf{x}$  is the state vector,  $\mathbf{u}$  is the input vector,  $\mathbf{y}$  is the output vector,  $F$  is the system matrix,  $G$  is the input matrix, and  $H$  is the output matrix. Note that the representation can be separated into two uncoupled modes representing the in-track ( $\dot{y}$  and  $y$ ) and cross-track ( $\dot{\phi}$ ,  $x$  and  $\phi$ ) motion, the latter being of prime interest.

Equations (6) and (7) are linearised and added to the output equation when using encoder measurements of the drive shafts' angular velocities.

### 3.4 Open-loop stability analysis

The study of the vehicle system's open-loop poles, though not ultimately decisive, provides valuable insights into the system's closed-loop performance. Here, in particular, vehicle parameters can be selected to make the open-loop poles more stable. Consider first the model with torque-inputs, for which  $\alpha$  (14) is the only non-zero pole. If the centre of mass ( $B^*$ ) is on the driving axle ( $B^*$  coincident with  $A$ , hence  $L_A - L_B = 0$ ), the system is marginally unstable (all poles in the left half plane or along the imaginary axis). If it is not, open-loop stability is a function of the sense of motion, determined by the sign of  $V_{j0}$ . Thus if ( $B^*$  is forward from  $A$  in the sense of motion, the system is marginally unstable (one or more poles in the right half plane). With  $B^*$  in the back, it is unstable. This difference in control stability can be given an experimental interpretation by observing the unforced motion of a supermarket cart, which is also a differential-drive type of system. As illustrated in Figure 3, when launched with an initial velocity, the system's centre of mass naturally tends to lead the driving axle. It follows that when the centre of mass is in the front, the trajectory is smooth. When it is in the back, the vehicle turns around.

**Figure 3** Experimental observation of a supermarket cart (a) in 'forward' motion, and (b) in 'backward' motion



For these reasons, we call ‘forward’ motion, the movement of the vehicle when  $B^*$  is in front of the driving axle. Hence the notions of front and back of the vehicle relative to  $B^*$ , in the direction of motion. Now that the nominal sense of motion is defined, the performance impact of moving  $B^*$  can be studied:  $B^*$  is best placed further forward from  $A$ . This may only be considered as a theoretical exercise since moving the centre of mass is a difficult task to realise in practice.

The same open-loop stability analysis is carried out for the system with voltage inputs. In this case there are two non-zero poles,  $\gamma$  (12) for the in-track mode and  $\alpha'$  (13) for the cross-track mode, both of which are functions of motor parameters. The mechanical constraints on the motors being more stringent than for other parameters, we use this study as a check. For the class of motors considered,  $\gamma$  is always negative. The same is true for  $\alpha'$ , but since it is a function of  $\alpha$ , the pole is more stable in forward motion than in backward motion. The resulting impact on the trajectory-tracking performance is simulated in the fifth section of this article.

For all the values simulated in the analysis, we verified that the system was fully controllable and observable. Note that there is one position of the GPS antenna for which the system is not fully observable:

$$L_S = L_A - \frac{V_{y0}}{\alpha'}.$$

This is not a critical issue here, since the system is not unstable. But combined unobservability and open-loop instability makes the performance error covariance grow unbounded, since no feedback error-correction is available. There may be cases, in other applications for example, for which this observation is critical. More details and explanations on this particular case are available in Joerger (2002).

## 4 Design of the controller

The design of the navigation, guidance and control system is based on modern control theory and uses the state space representation (10) and (11) derived in the previous section. The control system is a discrete-time closed-loop feedback algorithm using a linear quadratic regulator (LQR) and a Kalman filter. As opposed to traditional methods, a one time tuning of the controller’s elements is not sufficient here. Indeed, in the next section, we will analyse the system’s responses to variations in vehicle parameters. The controller must therefore account for changes in the vehicle’s configuration, so that systematic comparisons are fair.

### 4.1 The regulator

The derivation of the optimal LQR control gain is based on the minimisation of a cost function of the form:

$$J_c = \frac{1}{2} \int_0^{\infty} (\mathbf{x}^T Q_1 \mathbf{x} + \mathbf{u}^T Q_2 \mathbf{u}) d\tau.$$

The controller performance index weights (the coefficients of  $Q_1$  and  $Q_2$ ) are purposely distributed in the continuous rather than in the discrete formulation.



The process noise model is completed by considering a second source of disturbance: rotations of the drive motor shafts that do not necessarily generate a horizontal vehicle displacement, for example, in the case of a sudden obstacle in the ground, or of a loss of adherence on the wheels or on the reducers. Such disturbances are accounted for by assuming a random loss of angular velocity on the wheels. Therefore, the noise model establishes the effect on the states due to two gaussian random functions,  $\omega_{S\_R}(t)$  and  $\omega_{S\_L}(t)$ , respectively for the right and left wheel, both with spectral density  $\Omega_S$  (see Figure 4).

The derivation of the process noise vector is straightforward, and for small values of  $\theta_G$ ,  $\omega_{S\_R}$  and  $\omega_{S\_L}$ :

$$\delta\mathbf{x} = G_d\mathbf{w}(t) = \begin{bmatrix} -g \cos A_Z & 0 & 0 \\ (L_A - L_B) \frac{mg}{J_{ZZ}} \sin A_Z & 0 & 0 \\ 0 & 0 & 0 \\ 0 & R/2 & R/2 \\ 0 & -R/W & R/W \end{bmatrix} \begin{bmatrix} \theta_G(t) \\ \omega_{S\_R}(t) \\ \omega_{S\_L}(t) \end{bmatrix} \quad (15)$$

where  $G_d$  is the process noise input matrix, and  $\mathbf{w}(t)$  is the noise input vector. From the expression of  $G_d$ , it is evident that the disturbances have no direct effect on  $x$ , the third state. But integration over time of the noise vector  $\delta\mathbf{x}$  (necessary for discretisation, for example) shows that there is an accumulating effect on this particular state. The spectral density for the continuous random process is obtained by calculating the expected value of  $\delta\mathbf{x} \cdot \delta\mathbf{x}^T$ . The equivalent covariance matrix in the discrete domain can be computed using an algorithm due to Van Loan (Bryson, 2002), such that:

$$Q_d = \int_{T_s} e^{Ft} G_d R_w G_d^T (e^{Ft})^T dt, \quad (16)$$

with  $R_w = \begin{bmatrix} \Theta_G & 0 & 0 \\ 0 & \Omega_S & 0 \\ 0 & 0 & \Omega_S \end{bmatrix}$ , where  $R_w$  is the random noise functions' spectral density matrix.

The sensor noise for the DGPS sensor is modelled by two gaussian random functions with variance  $\sigma_{GPS}^2$ . The random functions noted  $v_{GPS\_X}(t)$  and  $v_{GPS\_Y}(t)$  account for measurement noises respectively in the  $x$  and  $y$  directions of the reference frame. Correlation over time, due to multipath effects, is modelled for each random function by a first order Markov process. Cross correlation between the two functions is assumed to be zero. We use state augmentation (Gelb, 1974), to account for coloured measurement noise in a second version of the controller, which we will refer to as the augmented controller. The noise for the encoder sensors is modelled with an uncorrelated gaussian random function with spectral density  $\sigma_{ENC}^2$ .

### 4.3 The closed-loop system

When adding the effects of external disturbances and sensor noise, the continuous-time model becomes:

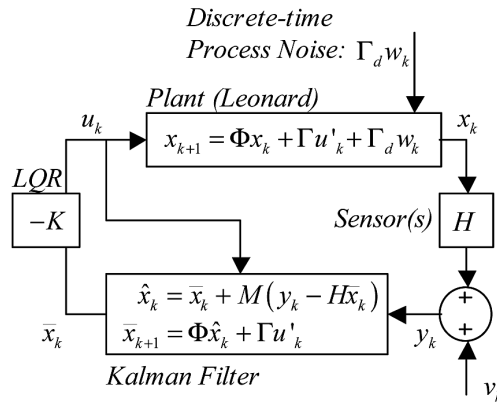
$$\dot{\mathbf{x}}(t) = F\mathbf{x}(t) + G\mathbf{u}(t) + G_d\mathbf{w}(t)$$

$$\mathbf{y}(t) = H\mathbf{x}(t) + \mathbf{v}(t)$$

where  $G_d\mathbf{w}(t)$  was expressed earlier, and  $\mathbf{v}(t) = \begin{bmatrix} v_{GPS-X}(t) \\ v_{GPS-Y}(t) \end{bmatrix}$ .

The discrete-time closed-loop controller is implemented as illustrated on the block diagram of Figure 5. Both the discrete optimal LQR gain ( $K$ ) and the discrete Kalman prediction estimator gain ( $M$ ) are computed based on a discretised version of the state space representation (Equations (10) and (11)). The sample time used for the discretisation is  $T_S$ , and corresponds to the sensor and actuator's update rates.

Figure 5 Block diagram for the covariance analysis



At this point of the process, parametric models for both the vehicle and the control system have been built, so that we can simulate their closed-loop trajectory-tracking performance as a function of relevant vehicle parameters.

### 5 Theoretical sensitivity analysis

At the climax of this work is the sensitivity analysis. We identify the effect of each system design parameter on the final path-following performance using a three-step process: covariance analysis to quantify performance sensitivity and bring the main trends into evidence; Monte-Carlo simulations (which use the full non-linear vehicle model and take into account the effects of drive motor saturation) to confirm these results; and experimental testing to provide the ultimate validation of the analysis and simulation results (Section 6).

Throughout the analysis, the trajectory-tracking performance index is chosen to be the standard deviation of the cross-track error on state  $x$ . A nominal configuration, defined at the bottom of Table 2, is used as reference for comparison when modifying parameters. The LQR controller's weights are tuned for this reference configuration, and left unchanged for the sensitivity analysis. A few experimental measurements of typical ground conditions are necessary to obtain a truthful process noise model. Using the resulting controller, a reference performance is obtained (Table 2, first row).

**Table 2** Summary of the simulated and experimental results (standard deviations in cm)

<i>Configuration studied</i>	<i>Covariance</i>	<i>Monte-Carlo</i>	<i>Experiment</i>
Nominal case	8.4	9.8	6.7
Driving backward	8.5	10.0	
Increasing $R_a$ , $k_T$ and $k_E$	9.2	11.7	
$B^*$ closer to $A$	6.8	8.6	
Best case ( $C = A$ , $S = front$ )	5.5	8.2	4.9
Worst case ( $C = front$ , $S = back$ )	23.2	36.1	43.3
$T_S = 1s$	16.9	20.0	20.1
With encoders	6.6	6.3	5.9
Worst case, with encoders	16.6	16.7	19.3
Augmented controller	5.3	7.4	6.5

Note: Nominal: forward motion,  $B^*$ ,  $S$  and  $C$  in the centre,  $T_S = 0.5s$

### 5.1 Simulations

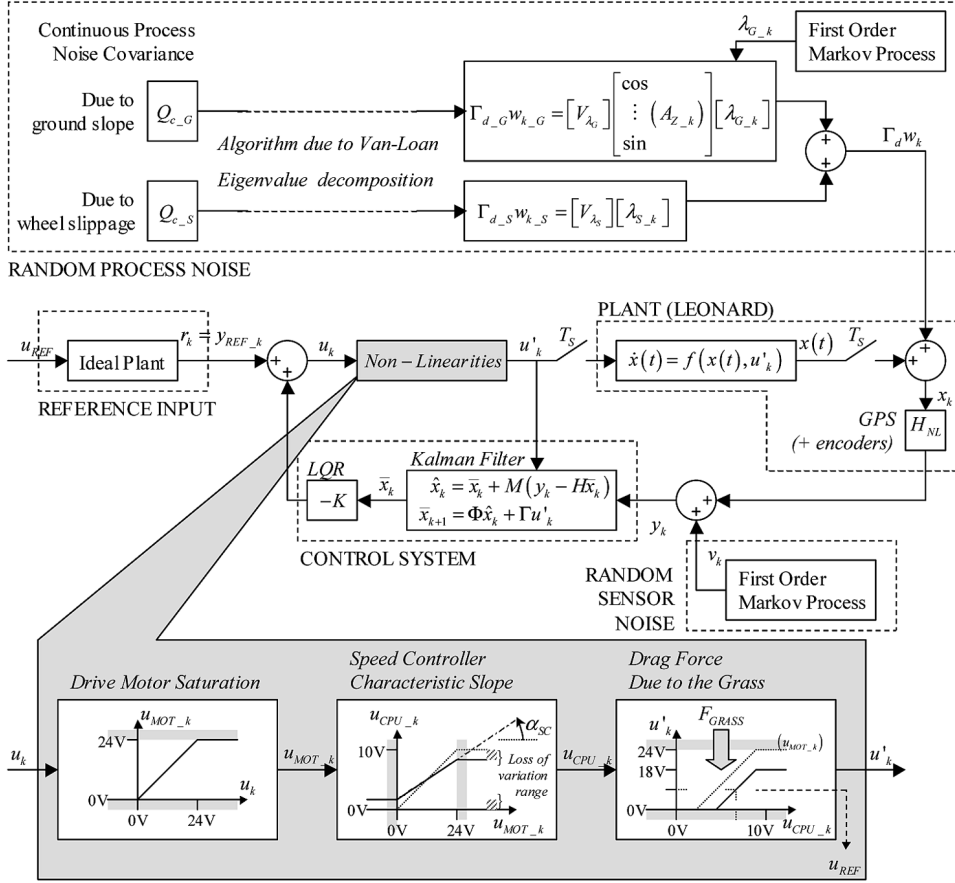
The covariance analysis is directly derived from the closed-loop system described Figure 5. It provides immediate performance predictions over the whole range of variation of each parameter. The ensemble-average mean-square performance of the closed-loop system is predicted using discrete Lyapunov Equations (Bryson, 2002).

When carrying out Monte-Carlo simulations, we can use a more complete model for the system, including non-linearities, and therefore give a more reliable estimate of the final performance. Nevertheless, the process is time-consuming, since it consists in estimating the ensemble-average vehicle path-tracking performance over numerous trials. Therefore only the main characteristics highlighted in the covariance analysis are simulated. The simulations are refined according to the parameter identification procedure described in Appendix 1, and further updated using experimental data.

A detailed block-diagram of the Monte-Carlo simulations is shown Figure 6. The controller is the same as in the covariance analysis. The reference input  $r_k$  is the output of an ideal plant operating at a nominal voltage  $u_{REF}$  (voltage necessary to operate at nominal velocity  $V_{y0}$ ). The non-linearities due to the motors' saturation regions, the speed controller's characteristic slope and the grass' drag force (identified in the next section) are accounted for in the corrected input voltage  $u'_k$  to the plant. The continuous non-linear equations of motion for the vehicle (Equations (1)–(3), (8) and (9)) are numerically integrated over each sample period to model the behaviour of the plant.

The derivation of the discrete-time random process noise vector  $\delta x_k$  requires several steps, as described in Appendix 2. Like the continuous-time model,  $\delta x_k$  accounts for disturbances due to the ground slope and wheel slippage. The random ground slope's correlation is modelled using a first order Markov process. The random azimuth,  $A_Z(k)$ , and the disturbances on the right and left wheels:  $\omega_{S-R}(k)$  and  $\omega_{S-L}(k)$ , are modelled as described for the continuous formulation (Section 4) with the appropriate distributions.

Figure 6 Block diagram of the simulated system



The sensor matrix  $H_{NL}$  is obtained from the non-linear Equations (4) and (5). Correlated sensor noise is introduced to the system as described in Section 4. The two versions of the control system, the unaugmented and the augmented controllers, are simulated and their performances are compared. (Recall that the augmented controller takes into account the correlation of the measurement noise.)

### 5.2 Results and analyses

The results of the simulations for various configurations are presented Table 2. Configurations of interest were selected according to the trends highlighted by the covariance analysis (second column).

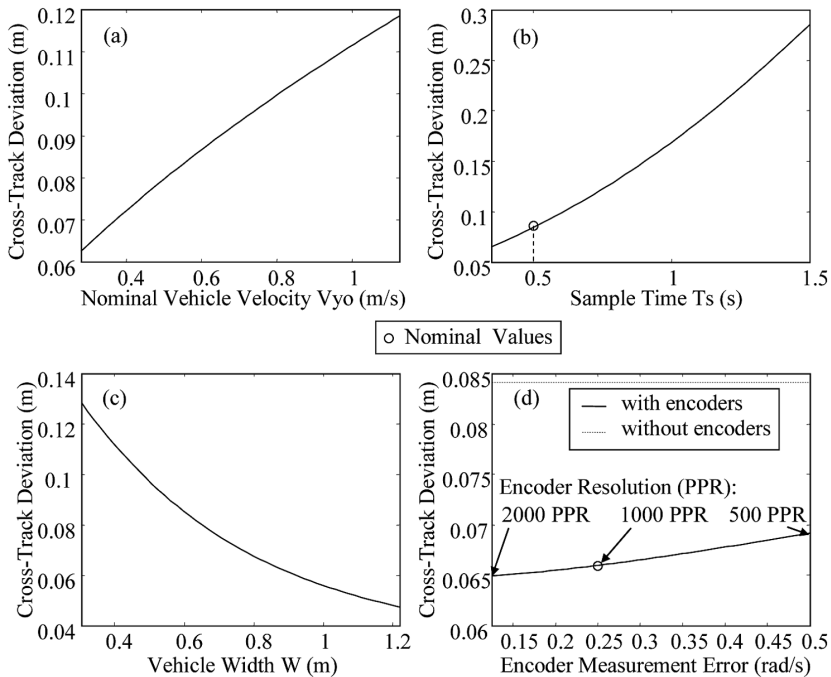
With the Monte-Carlo simulations, the performance of the closed-loop system is predicted with a higher degree of fidelity to the real physical system. The results of simulations of over 100 trials are given in Table 2 (third column), and confirm the linearisation hypotheses used for the covariance analysis. The differences with the covariance results stem from the added complexity in the Monte-Carlo simulations, in particular from the motor saturation.

5.2.1 General sensitivity analysis

First, the results described in Section 3.4 are confirmed. Rows 2 and 3 of Table 2 show the losses in performance observed when driving ‘backward’ and when selecting different motor windings (increasing  $R_a$ ,  $k_T$  and  $k_E$ ). We noted in Section 3.4 that these parameter modifications would make the open-loop poles less stable. Here we quantify the resulting effect on the closed-loop trajectory-tracking performance. In the same way, we saw that when the centre of mass  $B^*$  is closer to the driving axle (closer to  $A$ ), the open-loop poles are less stable. Therefore, for a given actuator effort, we could expect the closed-loop performance to get worse. Row 4 of Table 2 shows the opposite. The reason is that the sensitivity of the system to the external disturbances due to the ground slope increases as the distance between  $B^*$  and  $A$  increases (evident in the expression of  $G_d$  (15)). This characteristic outweighs the effect of a more stable open-loop pole, and  $B^*$  is best located close to  $A$ .

Then, there are several parameters for which we can anticipate the influence on the cross-track error, because of their obvious relationship to the system performance. For example, operating at lower nominal velocity ( $V_{y0}$ ) or at higher sample rate ( $1/T_S$ ) makes lateral trajectory corrections occur more frequently with respect to the distance travelled; a larger distance between the driving wheels ( $W$ ) increases the control sensitivity; and the addition of an auxiliary encoder sensor, described here for a range of resolution indexes, increases the accuracy of the state estimates. These trends are illustrated in Figure 7. The curves represent the cross-track error vs variations in the parameter of interest. They also illustrate how we chose these parameters, after selection of the actual vehicle components on the industrial market.

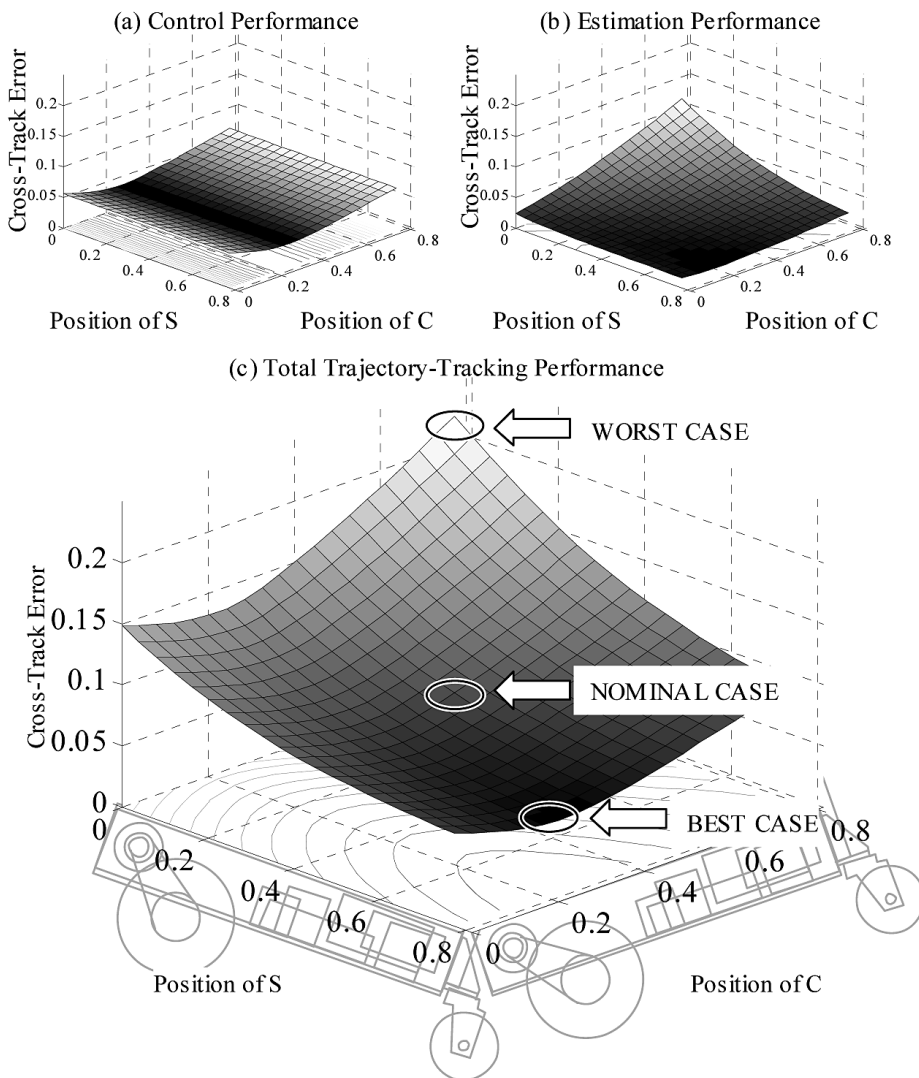
Figure 7 Covariance sensitivity analysis for (a)  $V_{y0}$ , (b)  $T_S$ , (c)  $W$ , (d)  $\sigma_{ENC}^2$



5.2.2 Influence of the control and sensor point

Finally, one of the most valuable aspects of this sensitivity analysis, is that it unveils the sometimes complex relationship between final performance and vehicle parameters. In this case, we are interested in the performance impact of the locations of the control point ( $C$ ) and of the sensor point ( $S$ ). An immediate result is that the relative position of those two points matters for the final performance as illustrated on the three-dimensional curve in Figure 8(c). Their individual impact can be studied by separating the ‘control performance’, which is a function of the location of  $C$  (Figure 8(a)), and the ‘estimation performance’, which is a function of  $S$  (Figure 8(b)).

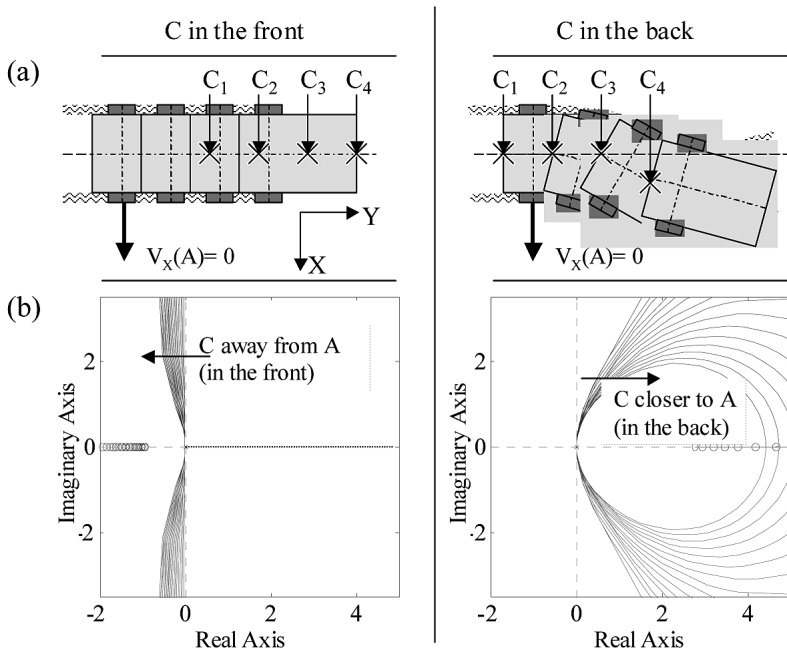
**Figure 8** (a) Impact of  $C$  on the ‘control performance’, (b) impact of  $S$  on the ‘estimation performance’, (c) combined impact of  $S$  and  $C$  on the total system performance



The control performance is the average cross-track error obtained when assuming full-state feedback with a perfect sensor. Figure 8(a) shows that the control performance is best when  $C$  is located on the driving axle ( $C$  and  $A$  coincident). The cross-track error increases slightly more rapidly as  $C$  is moved backward from  $A$  as opposed to forward from  $A$ .

Dramatic differences in the vehicle’s physical behaviour, depending on the position of  $C$ , are illustrated Figure 9. In both scenarios presented, we assume that the trajectory of point  $C$  is initially perfectly controlled and that there are no external disturbances. When point  $C$  is in the back, it can happen that although  $C$  remains centred on the trajectory, the vehicle’s heading angle deflects from its ideal value (first three time increments). In consequence, point  $C$  is quickly lead off-track (fourth increment), and the course correction causes a considerable cross-track error. In contrast, when  $C$  is in the front, no such correction is needed. Indeed, the dynamic model’s constraint Equation (3) imposes that the wheels do not slip laterally, so that unless there is some external disturbance, the heading angle remains at its ideal value.

**Figure 9** Performance impact of point  $C$  (a) on the system’s behaviour, (b) on the system’s root locus



Classical control theory is also useful to shed light on this problem. When studying the control performance (with full-state feedback), we can assimilate the vehicle to a single-input, single-output (SISO) system, with  $u_L - u_R$  as input and  $x$  as output. The resulting transfer function is expressed as:

$$TF_x(s) = \beta' \frac{-L_A \cdot s + V_{y0}}{s^2(s - \alpha')}$$

The three poles are independent of  $C$ . The zero is equal to  $V_{y0}/L_A$ , where  $L_A$  is the signed distance from  $C$  to  $A$ . Thus the value of the zero depends on  $C$ . We study the associated root loci while  $C$  is moved along the vehicle (Figure 9). When  $C$  is in the back of  $A$ , nearly the entire root locus (two out of three branches) is in the right half of the complex plane. However,  $C$  being forward enough from  $A$ , the root locus is wholly in the left half plane. Therefore locating the control point in the front of the vehicle has a beneficial impact on control performance.

The estimation performance is given by the covariance of the Kalman filter's state estimate. Figure 8(b) suggests that the antenna is best placed forward from the control point. Further analysis and experimental results show that the estimation of the heading angle  $\phi$  is made more difficult when the antenna is backward from  $C$ . Note that the variations in estimation performance are more significant in magnitude than the control performance.

### 5.2.3 Summary of the analysis

The total trajectory-tracking performance is a combination of both control and estimation performances as suggested Figure 8(c). The best result is obtained with the antenna in the far front of the vehicle and the control point slightly forward of the driving axle. The worst configuration is with  $S$  in the back and  $C$  in the front. Between those two cases, more than a 75% increase in performance is gained, which is most valuable given that there is almost no limiting mechanical constraint on the position of those two points. Notably, this increase in performance exceeds that provided by the additional use of encoder sensors with  $C$  and  $S$  at their worst case locations (see Table 2).

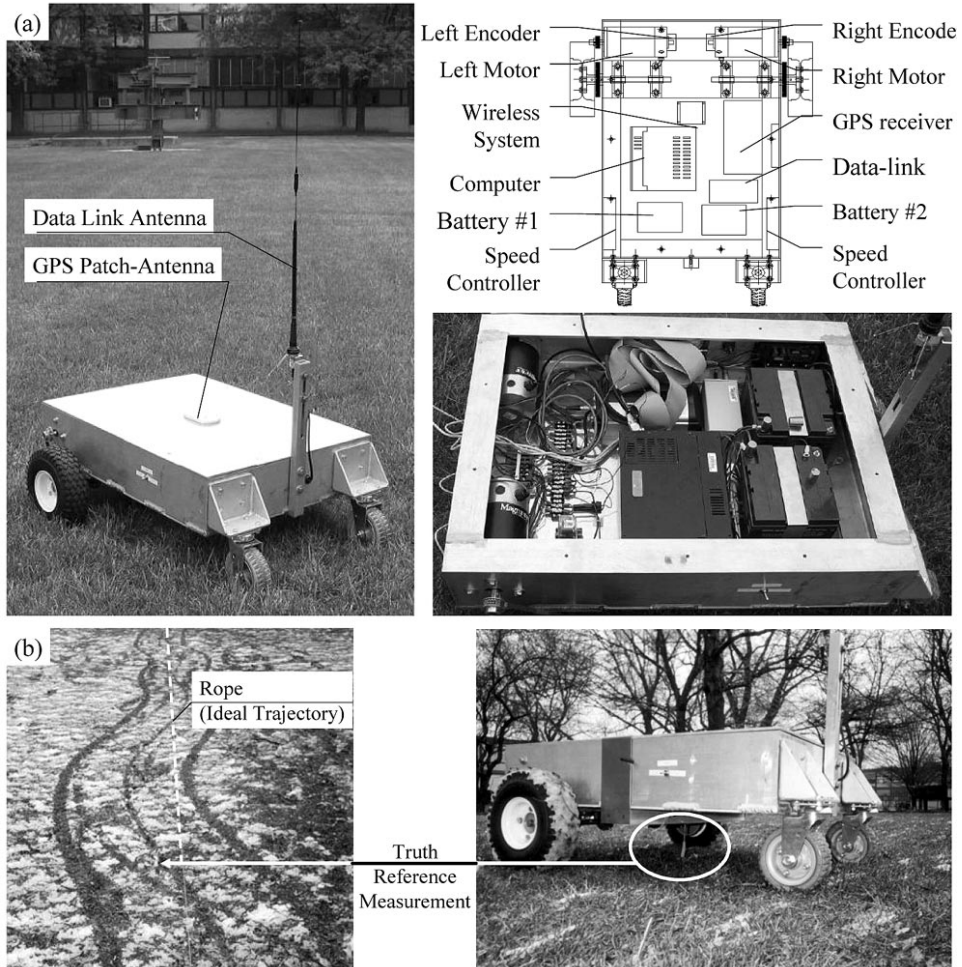
## 6 Experimental testing

The ultimate step of the sensitivity analysis is the experimental testing. Leonard has been tested in an open field after being designed according to the aforementioned procedure. Leonard's final assembly is illustrated Figure 10(a).

In order to validate the results of the sensitivity analysis, we need to carry out a series of tests while physically modifying design parameters. Unfortunately this is not always possible. For example, the influence of motors' characteristics or of the frame's width cannot be tested with the available equipment, which explains why the last column of Table 2 is not totally filled up. However, changing the position of the antenna or of the control point, or using encoder information, is easily realised. Note that when physically moving the GPS antenna, we include the aluminium plate (see Figure 10(a)) on which it is fixed, in order not to introduce undesired multipath effects.

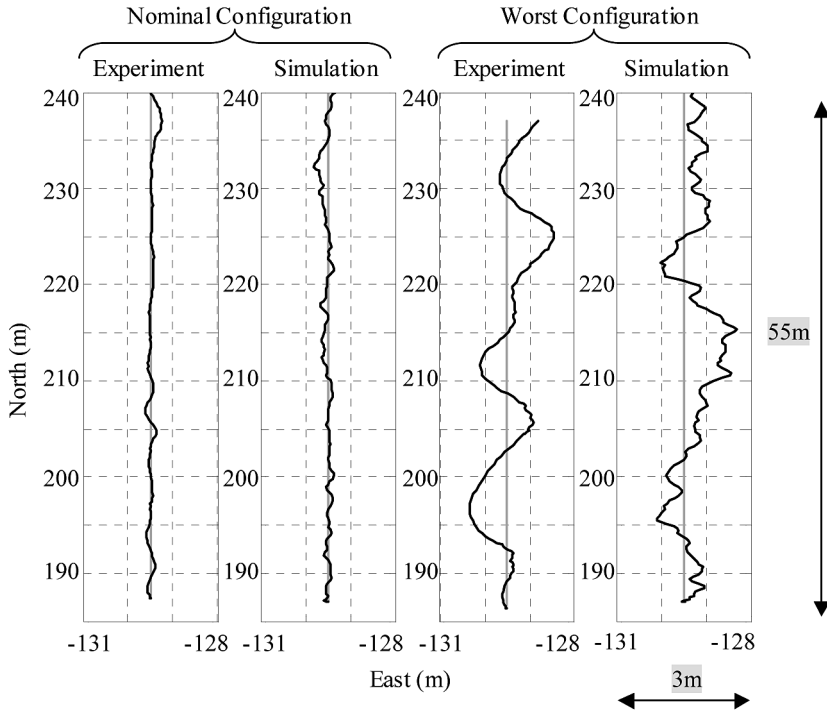
Truth reference position measurements are obtained by measuring, at regular intervals, the trace left in the snow by the vehicle with respect to an ideal linear trajectory, defined by a rope stretched in the North–South direction (Figure 10(b)). In order to observe accurately the trajectory of the control point  $C$ , a pointing stick was fixed at  $C$  and left a trace for the point of interest.

**Figure 10** (a) final vehicle assembly; and (b) truth reference measurement



For each configuration tested, we ran one 60 to 80 m long trial and calculated the standard deviation of the lateral error. The results, given in Table 2 (fourth column), are consistent with the covariance analysis and the Monte-Carlo simulation results. Experimental and simulated trajectories for the nominal and worst configurations are presented for comparison (Figure 11). Further calibration of simulation parameters would lead to a closer match between simulation and experiments, but the results are sufficiently accurate to highlight the desired trends. It is confirmed for example, that the path-tracking performance improves when the controller's update rate is increased. Also, in the worst case configuration for points *S* and *C*, the cross-track deviation is more than 30 cm, whereas in the optimal configuration, obtained by simply moving the GPS antenna, the error is less than 5 cm.

**Figure 11** Simulated and experimental trajectories



## 7 Conclusion

In this work, we have demonstrated and quantified the dramatic impact on the trajectory-tracking performance, of vehicle parameters that might be arbitrarily selected with traditional methods. In particular, different selections of the control point and GPS antenna locations alone generate variations in performance of up to 600%. When carefully chosen, however, the performance improvement realised is equivalent to that provided by the additional implementation of encoder sensors on the drive wheels.

In addition to the Leonard mobile platform, a reliable and flexible high-fidelity simulation has been built, experimentally calibrated, and validated. Accurate predictions are therefore easily and immediately available for future integrated AGV control system design applications.

## References

- Abbott, E. and Powell, D. (1999) 'Land-vehicle navigation using GPS', *Proceedings of the IEEE*, Vol. 87, No. 1, pp.145–162.
- Bell, T. (1999) 'Precision robotic control of agricultural vehicles on realistic farm trajectories', PhD thesis, Stanford University.
- Bryson, A.E. (2002) *Applied Linear Optimal Control*, Cambridge University Press.

- Bryson, A.E. and Ho, Y-C. (1975) ‘Optimal feedback control’, *Applied Optimal Control, Optimization, Estimation and Control*, Hemisphere Publishing Corp.
- Christ, J. (2003) ‘Development of an autonomous ground vehicle and implementation of a GPS-based navigation system’, MS thesis, Illinois Institute of Technology.
- Farrell, J.A., Han-Shue, T. and Yunchun, Y. (2003) ‘Carrier phase GPS-aided INS-based vehicle lateral control’, *Journal of Dynamic Systems, Measurement, and Control, Transactions of the ASME*, Vol. 125, pp.339–353.
- Gelb, A. (Ed) (1974) ‘Optimal linear filtering’, *Applied Optimal Estimation*, The MIT Press.
- Hannu, M. (2001) ‘Outdoor navigation of mobile robots’, PhD thesis, The Finnish Academies of Technology, Finland, pp.1–15.
- Joerger, M. (2002) ‘Development of a GPS-based navigation and guidance system for an automated ground vehicle’, MS thesis, Illinois Institute of Technology.
- Misra, P., Burke, B.P. and Pratt, M.M. (1999) ‘GPS performance in navigation’, *Proceedings of the IEEE*, Vol. 87, No. 1, pp.65–85.
- O’Connor, M. (1997) ‘Carrier-phase differential GPS for automatic control of land vehicles’, PhD thesis, Stanford University.
- Opshaug, G.R. and Enge, P. (2000) ‘Robotic snow cat’, *Proceedings of ION GPS 2000 the 13th International Technical Meeting of The Satellite Division of The Institute of Navigation*, Salt Lake City, UT.

## Appendix 1 Vehicle parameter identification

A parameter identification phase is useful to better estimate and model the actuator characteristics. The unloaded impulse response of the motor is modelled as a first-order system, such that:

$$\frac{\Omega(s)}{U(s)} = \frac{\frac{k_T}{k_T k_E + f_V R_a}}{1 + \frac{J R_a}{k_T k_E + f_V R_a} s} = \frac{K_{MOT\_SS}}{1 + \tau_{MOT} s}.$$

Motor specifications ( $k_T$ ,  $k_E$  and  $R_a$ ) are given by the manufacturer. The remaining unknowns are the equivalent inertia ( $J$ ) and viscous friction coefficient ( $f_V$ ) on the motor shaft due to the reducers and wheels. We therefore analyse the response of the unloaded motors to step inputs. Angular velocity measurements are taken on the motor shaft using encoders.  $J$  and  $f_V$  were deduced from measurements of the step-response steady-state value ( $K_{MOT\_SS}$ ) and time constant ( $\tau_{MOT}$ ) according to the preceding equation.

Voltages measured at the input and output of the speed controllers reveal an undesirable and unaccounted feature. As mentioned in Section 2, speed controllers send voltages to the motors proportionally to input voltages (coming from the computer). The proportionality relationship is determined by the speed controller’s characteristic slope, which is not necessarily tuned to the specific scales of the vehicle’s components. In this case, it further narrows down the actuators’ linear region. Corrections were made in the simulations and in Leonard’s feedback controller (Figure 9), such that the Kalman filter’s state prediction takes these effects into account. Also, steady-state responses to constant inputs were observed and analysed when the vehicle operated on various types of grounds. The measurements

show that there is a constant drag force acting on the wheels when the vehicle is driving on grass (probably the force necessary to bend the blades of grass). This drag force, as well as the re-evaluated saturation region, are used to determine the optimal operating point,  $u_{REF}$  (at the centre of the linear area), from which we deduce an updated reference input for the controller. Finally, to characterise the testing field and thus determine the process noise parameters, CDGPS measurements of the surface's altitude were taken. An average ground slope was deduced, as well as an average obstacle-height and obstacle-frequency per unit distance.

Table 3 summarises the vehicle and noise parameter values assigned for the reference configuration after selection of the vehicle components and identification of external elements.

**Table 3** Parameter values for the nominal configuration

Parameter	Value	Unit	Parameter	Value	Unit
$m$	82.74	kg	$R_a$	1.8	Ohms
$W$	0.610	m	$J$	0.0171	Nms <sup>2</sup>
$L$	0.914	m	$f_V$	0.0223	Nms
$R$	0.127	m	$T_S$	0.5	s
$L_A$	-0.203	m	$V_{y0}$	0.6	m/s
$L_B$	0	m	$\Theta_G$	1.5	deg
$L_S$	0	m	$\Omega_S$	10	deg/s
$N$	3.27		$\sigma_{GPS}$	0.02	cm
$k_T$	0.5176	Nm/A	$\sigma_{ENC}$	0.25	rad/s
$k_E$	0.5176	Vs			

## Appendix 2 Derivation of the discrete-time process noise vector

To simulate random disturbances, the continuous formulation (15) could not be used because we wanted to avoid integrating white noise over time. Also, there is no appropriate approximation to estimate the discrete-time random sequence:

$$\delta x_k = \Gamma_d w_k = \int_{T_s} e^{Ft} G_d w(t) dt,$$

since the system's time constants and the sample time are of the same magnitude. The alternative way is to use matrix decomposition (e.g. here, eigenvalue decomposition) to express the covariance of the discrete-time process noise  $Q_d$  in the form:

$$Q_d = \Gamma_d W_d \Gamma_d^T = V_\lambda \begin{bmatrix} \lambda_1^2 & & 0 \\ & \ddots & \\ 0 & & \lambda_3^2 \end{bmatrix} V_\lambda^T$$

where  $V_\lambda$  is a matrix of eigenvectors and  $\lambda_1^2$  are the eigenvalues, from which we deduce the discrete-time process noise vector:

$$\delta x_k = \Gamma_d w_k = V_\lambda \begin{bmatrix} \lambda_1^2 \\ \vdots \\ \lambda_5^2 \end{bmatrix}.$$

In consequence,  $w_k$  is now a five-by-one random vector with zero mean and variances  $(\lambda_1^2, \dots, \lambda_5^2)$ . Note that  $w_k$  is not the discrete-time representation of  $w(t)$  which was a three-by-one vector, but we ensure that the covariance of  $\delta x_k$  is  $Q_d$ . To further improve the relevance of the model, we simulate the randomness of the uniformly distributed azimuth of the slope,  $A_Z$ . First the contributions of the ground slope's disturbance ( $Q_{dG}$ ) and of sudden bumps or wheel slippage ( $Q_{dS}$ ) are separated (by use of Van Loan's algorithm to the appropriate components of the noise input matrix and vector in (15)):

$$Q_d = Q_{dG} + Q_{dS} = V_{\lambda_S} [\lambda_{Si}^2] V_{\lambda_S}^T + V_{\lambda_G} [\lambda_{Gi}^2] V_{\lambda_G}^T.$$

Then, for simplicity, assume the slope's azimuth is approximately constant over some time period  $T_{A_Z}$  determined experimentally, such that  $T_{A_Z} > T_S$ . The azimuth being constant over  $T_S$ , we can extract the terms functions of  $A_Z$  ( $\cos(A_Z)$  for the in-track mode and  $\sin(A_Z)$  for the cross-track mode) from the integral in (15) such that the disturbance vector becomes:

$$\delta x_k = \Gamma_d w_k = V_{\lambda_S} \begin{bmatrix} \lambda_{S1\_k} \\ \vdots \\ \lambda_{S5\_k} \end{bmatrix} + \begin{bmatrix} \cos(A_Z) & & 0 \\ & \ddots & \\ 0 & & \sin(A_Z) \end{bmatrix} V_{\lambda_G} \begin{bmatrix} \lambda_{G1\_k} \\ \vdots \\ \lambda_{G5\_k} \end{bmatrix}.$$

The random ground slope is modelled as a first order Markov process. Due to the eigenvalue decomposition of the covariance matrix, the expression of the variable representing the physical slope is no more apparent. But because the final result is representative of the experimental behaviour, we apply the Markov process to the square root of the eigenvalues ( $\lambda_{Gi\_k}$ ).